PERGAMON

International Journal of Plasticity 19 (2003) 647–674

INTERNATIONAL JOURNAL OF Plasticity

www.elsevier.com/locate/ijplas

Finite element modeling of plastic anisotropy induced by texture and strain-path change

Saiyi Li[a,*], Eric Hoferlin[a], Albert Van Bael[a], Paul Van Houtte[a], Cristian Teodosiu[b]

[a] *Department of Metallurgy and Materials Engineering, Katholieke Universiteit Leuven, Kasteelpark Arenberg 44, B-3001 Leuven, Belgium*

[b] *LPMTM-CNRS, Unversité Paris-Nord, Avenue J.-B. Clément, F-93430 Villetaneuse, France*

Received in final revised form 12 November 2001

Abstract

Consideration of plastic anisotropy is essential in accurate simulations of metal forming processes. In this study, finite element (FE) simulations have been performed to predict the plastic anisotropy of sheet metals using a texture- and microstructure-based constitutive model. The effect of crystallographic texture is incorporated through the use of an anisotropic plastic potential in strain-rate space, which gives the shape of the yield locus. The effect of dislocation is captured by use of a hardening model with four internal variables, which characterize the position and the size of the yield locus. Two applications are presented to evaluate the accuracy and the efficiency of the model: a cup drawing test and a two-stage pseudo-orthogonal sequential test (biaxial stretching in hydraulic bulging followed by uniaxial tension), using an interstitial-free steel sheet. The experimental results of earing behavior in the cup drawing test, maximum pressure and strain distribution in bulging, and transient hardening in the sequential test are compared against the FE predictions. It is shown that the current model is capable of predicting the plastic anisotropy induced by both the texture and the strain-path change. The relative significance of texture and strain-path change in the predictions is discussed.

Keywords: A. Microstructures; B. Anisotropic material; B. Crystal plasticity; C. Finite elements; Texture

1. Introduction

Finite element (FE) simulations of metal forming provide an effective means to investigate the relationship between processing deformation and structure, and

* Corresponding author. Tel.: +32-16-321781; fax: +32-16-321990.
E-mail address: sai-yi.li@mtm.kuleuven.ac.be (S. Li).

0749-6419/03/$ - see front matter
PII: S0749-6419(01)00079-1

therefore, useful guidance in the tuning of the production process. For many applications where a higher level of accuracy is desired, it is essential to dispose of a constitutive model that takes the plastic anisotropy of the material properly into account.

Crystallographic texture is the main source of the plastic anisotropy in forming processes without abrupt strain-path changes. Many efforts have been made in recent years to introduce such anisotropy into FE simulations (Mathur and Dawson, 1989; Van Houtte et al., 1989; Arminjon and Bacroix, 1991; Kalidindi et al., 1992; Chung and Shah, 1992; Beaudoin et al., 1993; Becker et al., 1993; Savoie and MacEwen, 1996). One of the proposed methods incorporates the texture-related crystal plasticity calculations directly into a FE analysis, relating each element to a polycrystalline aggregate (e.g. Becker et al., 1993). However, the extensive computing times involved for such calculations prevent it being used for detailed analyses of realistic forming processes. In another approach, an analytical function (called plastic potential) defined in strain-rate space is employed to describe the shape of yield locus (e.g. Van Houtte et al., 1989; Savoie and MacEwen, 1996). The coefficients of the plastic potential are determined by fitting to the crystal plasticity data obtained from the texture of the material. This approach in conjunction with isotropic hardening has been applied in FE modeling of the texture-induced anisotropy in sheet forming (e.g. Van Bael, 1994; Zhou et al., 1997, 1998; Li et al., 2000, 2001).

On the other hand, many experimental studies have shown that abrupt changes in strain-path, which are usual in multiple-stage forming processes, can also lead to plastic anisotropy following the transition (e.g. Ghosh and Backofen, 1973). The transition region is often characterized by an abrupt change of flow stress and work hardening rate, which have significant influence on the formability of the material. Rauch and Schmitt (1989) have shown that this kind of anisotropy results from the evolution of the microstructure, more precisely, the dislocation structure. Accordingly, different models, taking into account the dislocation structures and their evolutions at a macroscopic scale (Teodosiu and Hu, 1995) or microscopic scale (e.g. Rauch and Thuillier, 1993; Hoc and Forest, 2001; Langlois and Berveiller, in press), have been developed in order to predict the effect of strain-path changes. As shown by Hiwatashi et al. (1997,1998), the coupling between the anisotropic plastic potential of Van Houtte et al. (1989) and the microstructural hardening model of Teodosiu and Hu (1995) can lead to a better prediction of the forming limit strains under strain-path changes. Recently, this combined model has been implemented for implicit elastic–plastic FE simulations (see e.g. Hoferlin et al., 1999a, 2001).

The aim of the present study is to apply this combined constitutive model to investigate the effects of texture and strain-path changes on the plastic anisotropy in sheet metal forming. We first recapitulate the model as presented by Hiwatashi et al. (1997), including some recent developments. Then, the implementation of the model in implicit FE simulations is summarized. This is followed by the application of this model in the simulations of two typical tests: cup drawing test and two-stage pseudo-orthogonal sequential test. The former demonstrates the ability to compute the anisotropic deformation mainly arising from the crystallographic texture. The latter illustrates the ability to predict the transient hardening resulting from the

microstructure evolution under strain-path change. The accuracy and the efficiency of the model are evaluated in comparison with other simple constitutive models, which are constructed by considering the effects of texture or microstructural hardening alone or not at all.

Regarding notation, tensors are denoted by boldface characters and tensor products are denoted by $\otimes$. The superposed dot denotes the material time derivative, and the prefix tr indicates the trace. In addition, $\boldsymbol{\delta}$ and $\mathbf{I}$ are the second- and fourth-order identity tensors respectively.

2. Constitutive model

2.1. Framework

The present constitutive model is a physics-based, phenomenological model. The evolution of flow stress is described by the yield locus constructed on the basis of crystal plasticity theory and microstructural observations. The shape of the yield locus can be generated from the crystallographic texture measured by e.g. X-ray or neutron diffraction. In the present study, texture evolution during plastic deformation is neglected, although it should be taken into account in future development. Hence, the shape of the yield locus depends only on the initial texture and does not change. For well-annealed metals, the center of the yield locus of the virgin material is supposed to be at the origin of the stress space. The position and the size of the yield locus during deformation correspond to its translation and isotropic expansion, and therefore characterize respectively the kinematic and isotropic hardening.

In this framework, the rate of plastic work per unit volume $\dot{W}$ for a given plastic strain-rate $\dot{\boldsymbol{\varepsilon}}^{\mathrm{p}}$ can be decomposed into a term associated with the kinematic hardening $\dot{W}_{\mathrm{k}}$ (associated with the backstress $\mathbf{X}$) and a term associated with the isotropic hardening $\dot{W}_{\mathrm{i}}$, i.e.

$$\dot{W} = \dot{W}_{\mathrm{k}} + \dot{W}_{\mathrm{i}} \tag{1}$$

with

$$\dot{W}_{\mathrm{k}} = \mathbf{X} : \dot{\boldsymbol{\varepsilon}}^{\mathrm{p}} \tag{2}$$

The term $\dot{W}_{\mathrm{i}}$ will be formulated through the use of the texture-based anisotropic plastic potential in the following section. The backstress $\mathbf{X}$ will be described in Section 2.3.

2.2. Texture-based plastic potential in strain-rate space

The Taylor–Bishop–Hill (TBH) theory has been recognized as one of the most successful crystal plasticity models that can provide a comprehensive and low-cost way of deriving the shape of the yield locus of a polycrystalline material from its

crystallographic texture (Van Houtte et al., 1989). Assuming that the plastic deformation at room temperature is envisaged to occur as multiple slip, the internally dissipated frictional work rate in each grain with a crystallographic orientation $\mathbf{g}$ (represented by three Euler angles known as φ_1, Φ and φ_2 in the Euler space) can be written as

$$\dot{w}_\mathrm{i} = \tau \sum_\mathrm{s} \dot{\gamma}_\mathrm{s} = \mathrm{Min}, \tag{3}$$

where τ is the critical resolved shear stress (CRSS) which is assumed to be identical in every slip system, and $\dot{\gamma}_\mathrm{s}$ the slip rate in each slip system s. In the TBH theory, the local plastic strain-rate tensor that describes the deformation of the individual crystallites is assumed to be equal to the prescribed macroscopic plastic strain-rate $\dot{\boldsymbol{\varepsilon}}^\mathrm{p}$. The active slip systems and the corresponding slip rates can be calculated in such way that they together achieve the plastic strain-rate $\dot{\boldsymbol{\varepsilon}}^\mathrm{p}$ with a minimum $\dot{w}_\mathrm{i}$.

By defining the Taylor factor as

$$M = \frac{\dot{w}_\mathrm{i}}{\tau \dot{\varepsilon}^\mathrm{p}_\mathrm{vm}}, \tag{4}$$

where $\dot{\varepsilon}^\mathrm{p}_\mathrm{vm}$ $(= \sqrt{\frac{2}{3}}\sqrt{\dot{\boldsymbol{\varepsilon}}^\mathrm{p} : \dot{\boldsymbol{\varepsilon}}^\mathrm{p}} = \sqrt{\frac{2}{3}}\dot{\varepsilon}^\mathrm{p}$, $\dot{\varepsilon}^\mathrm{p}$ denotes the norm of $\dot{\boldsymbol{\varepsilon}}^\mathrm{p}$) is the von Mises equivalent plastic strain-rate, the internally dissipated frictional work rate over the polycrystalline material can be represented by

$$\dot{W}_\mathrm{i} = \tau \dot{\varepsilon}^\mathrm{p}_\mathrm{vm} \bar{M}(\mathbf{A}). \tag{5}$$

$\bar{M}(\mathbf{A})$ is the average Taylor factor calculated as a function of $\mathbf{A}$, i.e. the mode of the plastic strain-rate ($\mathbf{A} = \dot{\boldsymbol{\varepsilon}}^\mathrm{p}/\dot{\varepsilon}^\mathrm{p}$). It is given by:

$$\bar{M}(\mathbf{A}) = \int f(\mathbf{g}) M(\mathbf{g}, \mathbf{A}) \mathrm{d}\mathbf{g} \tag{6}$$

using the orientation distribution function (ODF) $f(\mathbf{g})$, representative of the texture of the material. For a particular sample with a known ODF, $\bar{M}$(A) can be calculated in a very efficient way from the database of Taylor factors $M(\mathbf{g},\mathbf{A})$, which are calculated once and for all for a large number of crystal orientations $\mathbf{g}$ and for a large number of strain-rate modes $\mathbf{A}$.

It is clear from Eq. (5) that $\dot{W}_\mathrm{i}$ can be considered as a function of $\dot{\boldsymbol{\varepsilon}}^\mathrm{p}$ only, and be used as a plastic potential in the strain-rate space, on condition that $\bar{M}$ is written as a function of $\mathbf{A}$. For materials that are plastically incompressible and rate-insensitive, the effective deviatoric stress (corresponding to isotropic hardening) can be derived from the plastic potential by the normality rule (Van Houtte et al., 1992; Van Houtte, 1994):

$$\mathbf{u} = \frac{\partial \dot{W}_\mathrm{i}}{\partial \dot{\boldsymbol{\varepsilon}}^\mathrm{p}}. \tag{7}$$

Here, the partial derivations are performed after converting the deviatoric stress and the strain-rate tensors into five-dimensional vectors. This makes necessary the conversion from the double index ij ($i, j = 1, 2, 3$) for the tensor components into a single index p which ranges from 1 to 5 for the vector components, as explained in Van Houtte et al. (1992).

As the equation for $\dot{W}_i$ [Eq. (5)] contains the texture-dependent function $\bar{M}(\mathrm{A})$, which is only known for a finite number of strain-rate modes **A**, an interpolation scheme for intermediate strain-rate modes is needed if Eq. (7) must be evaluated. A practical way of doing this is to fit an analytical function, say $Q(\mathbf{A})$, to $\sqrt{\frac{2}{3}}\bar{M}(\mathbf{A})$. $Q(\mathbf{A})$ is represented by a polynomial series expansion defined in the strain-rate space (Van Houtte et al., 1992), i.e.

$$Q(\mathbf{A}) = F_{p_1 p_2 \ldots p_N} A_{p_1} A_{p_2} \ldots A_{p_N} \tag{8}$$

with $1 \leqslant p_1 \leqslant p_2 \leqslant \ldots \leqslant p_N \leqslant 5$, using the vector representation of the strain-rate mode **A** as mentioned above. The subscript N depicts the order of the series expansion. There are, for example, 210 $F_{p_1 p_2 \ldots p_N}$ coefficients for a 6th-order series expansion.

Replacing $\bar{M}(\mathbf{A})$ by $Q(\mathbf{A})$ and $\dot{\varepsilon}^{\mathrm{p}}_{\mathrm{vm}}$ by $\dot{\varepsilon}^{\mathrm{p}}$, (5) can be recast as

$$\dot{W}_i = \tau \dot{\varepsilon}^{\mathrm{p}} Q(\mathbf{A}) \text{ or } \dot{W}_i = \tau \dot{\Gamma} \tag{9}$$

with

$$\dot{\Gamma} = \dot{\varepsilon}^{\mathrm{p}} Q(\mathbf{A}). \tag{10}$$

$\dot{\Gamma}$ Represents the average slip rate over the polycrystal and serves as a work-equivalent measure of the plastic strain-rate $\dot{\boldsymbol{\varepsilon}}^{\mathrm{p}}$. The plastic potential as represented by degenerates to the dual potential of the von Mises yield criterion if $Q(\mathbf{A}) = \sqrt{\frac{2}{3}}$.

Then, substituting Eq. (9) into Eq. (7), one has:

$$\mathbf{u} = \tau \mathbf{U} \tag{11}$$

where **U** is the normalized effective deviatoric stress tensor, given by

$$\mathbf{U} = \frac{\partial[\dot{\varepsilon}^{\mathrm{p}} Q(\mathbf{A})]}{\partial \dot{\boldsymbol{\varepsilon}}^{\mathrm{p}}} = \frac{\partial[\dot{\Gamma}(\dot{\boldsymbol{\varepsilon}}^{\mathrm{p}})]}{\partial \dot{\boldsymbol{\varepsilon}}^{\mathrm{p}}} \tag{12}$$

According to its dimensionless nature, **U** represents the shape of the yield locus.

Finally, it is easy to demonstrate from Eqs. (1), (2), (9), and (12), that the deviatoric stress associated with both the kinematic and the isotropic hardening can be given by

$$\hat{\boldsymbol{\sigma}} = \frac{\partial \dot{W}}{\partial \dot{\boldsymbol{\varepsilon}}^{\mathrm{p}}} = \frac{\partial(\dot{W}_{\mathrm{k}} + \dot{W}_{\mathrm{i}})}{\partial \dot{\boldsymbol{\varepsilon}}^{\mathrm{p}}} = \frac{\partial[\mathbf{X} : \dot{\boldsymbol{\varepsilon}}^{\mathrm{p}} + \tau \dot{\varepsilon}^{\mathrm{p}} Q(\mathbf{A})]}{\partial \dot{\boldsymbol{\varepsilon}}^{\mathrm{p}}} = \mathbf{X} + \tau \mathbf{U} \tag{13}$$

In this expression, $\mathbf{X}$ and τ characterize, respectively, the center and the size of the yield locus. They are associated with the microstructural evolution that will be addressed in the next section.

2.3. Microstructure-based hardening

The plastic behavior of metals depends not only on the current state of deformation, but also on the deformation history. The influence of the deformation history can be reasonably represented by a sufficient number of microstructural parameters, called internal variables. The microstructural hardening model presented in this section was originally proposed for steels with three internal variables, in order to incorporate the anisotropic work-hardening under arbitrary strain-path changes at moderately large strains (Hu, 1994; Teodosiu and Hu, 1995). Microscopic evidence is used as a hint for choosing adequate internal variables and for postulating their evolution equations.

The complete set of internal variables of the present microstructural hardening model is denoted by (R, $\mathbf{X}$, $\mathbf{S}$, $\mathbf{P}$). For a well-annealed material, all their initial values are zero. The scalar variable R describes the isotropic hardening produced beyond the yield limit by the statistically accumulated dislocations (Haddadi et al., 1999). For convenience its initial value is always taken equal to zero, because any initial work hardening can be incorporated in the initial yield stress. Note that this internal variable did not appear in the previous version of the model (Hiwatashi et al., 1997). The backstress $\mathbf{X}$, a second-order tensor, denotes the kinematic hardening. The internal variable $\mathbf{S}$, a fourth-order tensor, describes the directional strength of persistent dislocation structures (PDSs). It is the most important descriptor of the microstructural organization of interest. The choice of its order is due to the necessity to describe the anisotropic contribution of dislocation structures to the flow stress. The internal variable $\mathbf{P}$, a second-order tensor, is associated with the polarity of the PDSs, which is due to the excess of dislocations of the same sign on each side of a dislocation sheet. In what follows, all tensorial variables will be considered co-rotational with the material, while their objective rates (denoted by a small superposed circle) will be of Jaumann type, in order to take into account the large rotation effects (see e.g. Teodosiu and Hu, 1995).

The evolution of the internal variable R is represented by

$$\dot{R} = C_{\mathrm{R}}(R_{\mathrm{sat}} - R)\dot{\Gamma}, \tag{14}$$

where C_{R} characterizes the rate of the isotropic hardening produced by the statistically distributed dislocations and R_{sat} is the saturation value of R.

The evolution equation of the polarity tensor $\mathbf{P}$ can be written as

$$\overset{\circ}{\mathbf{P}} = C_{\mathrm{P}}(\mathbf{A} - \mathbf{P})\dot{\Gamma}, \tag{15}$$

where C_P characterizes the polarization rate of the PDS. Whatever the initial value of $\mathbf{P}$, its norm P will approach unity and $\mathbf{P}$ will tend to $\mathbf{A}$, whenever the strain-rate direction $\mathbf{A}$ remains unchanged for an amount of deformation that is sufficiently large with respect to $1/C_P$.

The evolution of $\mathbf{X}$ is associated with the process of dislocation pile-up. It tends to converge asymptotically towards a saturation function $\mathbf{X}_{sat}$ according to the following equation

$$\overset{\circ}{\mathbf{X}} = C_X(\mathbf{X}_{sat} - \mathbf{X})\dot{\Gamma}, \tag{16}$$

where C_X characterizes the saturation rate of $\mathbf{X}$. Furthermore, $\mathbf{X}$ is supposed to asymptotically become coaxial with $\mathbf{U}$ and therefore $\mathbf{X}_{sat}$ is assumed to be parallel to $\mathbf{U}$, i.e.

$$\mathbf{X}_{sat} = X_{sat}\mathbf{U}. \tag{17}$$

where X_{sat} is the saturation value of X (the norm of $\mathbf{X}$). In general, C_X has a relatively high value, and hence $\mathbf{X}$ approaches very rapidly its saturation value. From the mathematical point of view, X_{sat} should be a function of the scalar invariants generated by $\mathbf{S}$ and $\mathbf{A}$. Thus, the backstress $\mathbf{X}$ will describe not only the rapid variations of the flow stress following strain-path change, but also the new stationary states that are asymptotically approached afterwards. It is assumed that

$$X_{sat} = X_0 + (1-m)\sqrt{\lambda S^2 + (1-\lambda)S_D^2}, \tag{18}$$

where X_0 is the initial value of X_{sat}, λ is a material parameter describing the relative stronger contribution of the latent dislocations than that of the currently active dislocations, and

$$S_D = \mathbf{A} : \mathbf{S} : \mathbf{A}. \tag{19}$$

is the strength of the dislocation structures associated with the currently active slip systems. The second term in Eq. (18) corresponds to the effect of the planar PDS's as represented by the internal variable $\mathbf{S}$, and $(1-m)$ denotes the contribution of the intragranular structure to the kinematic hardening.

When a metal is deformed from a well-annealed initial state, dislocation sheets or cells develop roughly parallel to the active slip planes. On the other hand, for a severely cold-deformed material subjected to a subsequent orthogonal deformation, the strain-rate is highly localized. The microbands are parallel to the newly active slip planes, and between them new dislocation sheets are gradually formed (Rauch and Schmitt, 1989). This experimental evidence strongly suggests that dislocation structures associated with the current direction of the strain-rate evolve quite differently from the rest of the PDSs. In order to describe such evolution processes, and taking into account the definition of S_D [Eq. (19)], $\mathbf{S}$ is decomposed as

$$\mathbf{S} = S_{\mathrm{D}}\mathbf{A} \otimes \mathbf{A} + \mathbf{S}_{\mathrm{L}}, \tag{20}$$

where $\mathbf{S}_{\mathrm{L}}$ is associated with the latent part of the dislocation structures.

The evolution of S_{D} is given by

$$\dot{S}_{\mathrm{D}} = C_{\mathrm{SD}}[h_{\mathrm{P}}(S_{\mathrm{sat}} - S_{\mathrm{D}}) - h_{\mathrm{X}} S_{\mathrm{D}}]\dot{\Gamma}, \tag{21}$$

where C_{SD} and S_{sat} characterize, respectively, the saturation rate and the saturation value of S_{D}. The parameter h_{P} describes the influence of the polarity and is a function of S_{D} and $\mathbf{P} : \mathbf{A}$, i.e.

$$h_{\mathrm{P}} = \begin{cases} 1 - \dfrac{C_{\mathrm{P}}}{C_{\mathrm{SD}} + C_{\mathrm{P}}} \left| \dfrac{S_{\mathrm{D}}}{S_{\mathrm{sat}}} - \mathbf{P} : \mathbf{A} \right| & \text{if } \mathbf{P} : \mathbf{A} \geqslant 0 \\ (1 - \mathbf{P} : \mathbf{A})^{n_{\mathrm{P}}} \left(1 - \dfrac{C_{\mathrm{P}}}{C_{\mathrm{SD}} + C_{\mathrm{P}}} \dfrac{S_{\mathrm{D}}}{S_{\mathrm{sat}}} \right) & \text{otherwise} \end{cases} \tag{22}$$

and h_{X} is a function of $\mathbf{X} : \mathbf{A}$, defined as

$$h_{\mathrm{X}} = \frac{1}{2}\left(1 - \frac{\mathbf{X} : \mathbf{A}}{X_{\mathrm{sat}} Q} \right). \tag{23}$$

As has been shown in Hu (1994), the presence of h_{X} enables to evaluate the slight loss of S_{D} as $\mathbf{X}$ approaches its saturation value.

The evolution of $\mathbf{S}_{\mathrm{L}}$ results from the interaction between microbands and the preformed microstructures. Two physical mechanisms are possible: the annihilation of dislocations in the preformed structures, as proposed by Thuillier and Rauch (1994), and the softening of the preformed structure after being sheared by microbands, as implicitly suggested by Bay et al. (1992). Both mechanisms reduce the strength of the preformed structures as represented by S_{L}. Hence, the following evolution equation is used to describe these phenomena:

$$\overset{\circ}{\mathbf{S}}_{\mathrm{L}} = C_{\mathrm{SL}} \left(\frac{S_{\mathrm{L}}}{S_{\mathrm{sat}}} \right)^{n_{\mathrm{L}}} \mathbf{S}_{\mathrm{L}} \dot{\Gamma}, \tag{24}$$

where n_{L} is a positive material parameter. The term $(S_{\mathrm{L}}/S_{\mathrm{sat}})^{n_{\mathrm{L}}}$ is introduced in order to explain the influence of the amount of prestrain. According to Rauch and Schmitt (1989), for a severely deformed material under a subsequent orthogonal deformation, the percentage of grains containing microbands increases with the prestrain. Since the diminution of S_{L} is mainly due to the interaction between microbands and preformed microstructures, the decreasing rate of S_{L} should increase with prestrain. When the prestrain is small, $(S_{\mathrm{L}}/S_{\mathrm{sat}})^{n_{\mathrm{L}}} \ll S_{\mathrm{sat}}$, hence the evolution of S_{L} is

negligible, whereas when the prestrain is large, it approaches S_{sat}, and the evolution of S_L is speeded up.

Finally, accounting for the isotropic hardening produced beyond the yield limit by both the statistically accumulated dislocations and the PDSs, the size of the yield locus can be calculated as

$$\tau = \tau_0 + R + mS, \tag{25}$$

where τ_0 is the initial value of τ and $S = \sqrt{S_D^2 + S_L^2}$. The parameter m denotes the contribution of $\mathbf{S}$ to the isotropic hardening.

2.4. Combined models and identification of material parameters

The combination of the texture-based yield locus and the microstructural hardening model as stated above leads to an advanced constitutive model, say Tex–Mic. While this model will be used intensively in the present investigation, the following three models have also been used in the present work: (1) Von–Iso model: a combination of the von Mises yield locus and isotropic hardening; (2) Von–Mic model: a combination of the von Mises yield locus and the microstructural hardening model; (3) Tex–Iso model: a combination of the texture-based anisotropic yield locus and isotropic hardening. With these four models, the effect of texture and/or microstructural hardening can be readily evaluated. For example, a comparison of two simulations performed by use of the Tex–Mic and the Von–Mic models respectively, would expose the significance of the texture when microstructural hardening has been taken into account. A comparison of two simulations performed by use of the Tex–Mic and Tex–Iso models respectively, would reveal the influence of the microstructural hardening when the texture has been considered.

The Tex–Mic model involves a total of 13 material parameters, namely τ_0, X_0, R_{sat}, S_{sat}, C_P, C_R, C_{SD}, C_{SL}, C_X, m, λ, n_L and n_P. In practice, the identification of material parameters are first carried out for the Von–Mic model with the aid of a set of mechanical tests. It includes seven monotonic tests of uniaxial tension carrying out at 0, 15, 30, 45, 60, 75 and 90° to RD, eight monotonic tests of simple shear carrying out at 0, 30, 45, 60, 90, 120, 135 and 150° to RD, three Bauschinger sequence tests of simple shear involving 10, 20 and 30% amount of forward shear, and two orthogonal sequence tests realized by first imposing a true tensile strain of 10 or 20% in the rolling direction (RD) and then shearing in the same direction (Haddadi et al., 1999). To account for the influence of the planar anisotropy in the sheet, the results for the monotonic tests at various directions with respect to RD are averaged before carrying out the identification procedures.

Then, the material parameters for the Tex–Mic model can be converted from those for the Von–Mic model, accounting for the difference between the isotropic and the anisotropic yield loci. The conversion procedure used here is based on the consideration that both models should produce the same uniaxial tensile curve along RD. Let $\tau_{Von–Mic}$ and $\tau_{Tex–Mic}$ be the CRSS's conjugate, respectively, to $\dot{\Gamma}_{Von–Mic}$ and $\dot{\Gamma}_{Tex–Mic}$, the work-equivalent measures of the plastic strain-rate, the following equation holds according to Eq. (9):

$$\tau_{\text{Von–Mic}}\dot{\Gamma}_{\text{Von–Mic}} = \tau_{\text{Tex–Mic}}\dot{\Gamma}_{\text{Tex–Mic}} \tag{26}$$

For the case of uniaxial tension, Eq. (10) gives:

$$\dot{\Gamma}_{\text{Von–Mic}} = \dot{\varepsilon}^{\text{p}}_{11}, \dot{\Gamma}_{\text{Tex–Mic}} = \dot{\varepsilon}^{\text{p}}_{\text{UT}} Q_{\text{UT}} = \sqrt{1 + (-q_{\text{UT}})^2 + (q_{\text{UT}} - 1)^2}\,\dot{\varepsilon}^{\text{p}}_{11} Q_{\text{UT}} \tag{27}$$

Here, Q_{UT} and q_{UT} are respectively the value of the series expansion and the contraction ratio between the width and length plastic strains, corresponding to uniaxial tension. Both can be readily derived from the plastic potential representative of the texture of the material.

Substituting Eq. (27) into Eq. (26), one has:

$$\tau_{\text{Tex–Mic}} = \frac{\tau_{\text{Von–Mic}}}{\text{y}} \tag{28}$$

with

$$y = \sqrt{1 + (-q_{\text{UT}})^2 + (q_{\text{UT}} - 1)^2}\,Q_{\text{UT}}. \tag{29}$$

It is then easy to show that the parameters τ_0, X_0, R_{sat}, S_{sat}, C_{P}, C_{R}, C_{SD}, C_{SL}, C_{X} for the Tex–Mic model can be determined by dividing the corresponding value for the Von–Mic model by the conversion factor y, according to the expression of τ [Eq. (25)] and other equations involved. Meanwhile, the values for the rest of the material parameters remain the same for both models.

Analogously, the conversion of material parameters between the Von–Iso and Tex–Iso models can also be performed. Firstly, the isotropic hardening law employed in the Von–Iso model is represented by a Swift-type form

$$\sigma_{11} = k\left(\varepsilon^{\text{p}}_0 + \varepsilon^{\text{p}}_{11}\right)^n, \tag{30}$$

where σ_{11} and $\varepsilon^{\text{p}}_{11}$ are respectively the uniaxial stress and plastic strain during uniaxial tensile test. The parameters k, ε^{p}_0 and n are reference stress, offset plastic strain and hardening exponent, respectively. Their values can be determined by fitting the equation to the experimental tensile stress-strain curve for a tensile test along RD.

On the other hand, the isotropic hardening law for the Tex–Iso model can also be represented by a Swift-type form, using the same hardening exponent (n) as for the Von–Iso model:

$$\tau = k'(\Gamma_0 + \Gamma)^n. \tag{31}$$

Applying Eq. (9) to the case of uniaxial tension for the Von–Iso and the Tex–Iso models respectively, one obtains:

$$k\left(\varepsilon^{\text{p}}_0 + \varepsilon^{\text{p}}_{11}\right)^n \dot{\varepsilon}^{\text{p}}_{11} = k'(\Gamma_0 + \Gamma)^n \dot{\Gamma} \tag{32}$$

Meanwhile, applying Eq. (10) to uniaxial tension for the Tex–Iso model, the work-equivalent measure of the plastic strain-rate can be written as

$$\dot{\Gamma} = \sqrt{1 + (-q_{\mathrm{UT}})^2 + (q_{\mathrm{UT}} - 1)^2}\,\dot{\varepsilon}^{\mathrm{p}}_{11} Q_{\mathrm{UT}} = y\dot{\varepsilon}^{\mathrm{p}}_{11}. \tag{33}$$

Assuming $\Gamma = \int \dot{\Gamma}\mathrm{d}t$, we simply have

$$\Gamma_0 = y\varepsilon^{\mathrm{p}}_0, \Gamma = y\varepsilon^{\mathrm{p}}_{11}. \tag{34}$$

Then, by substituting Eqs. (33) and (34) into Eq. (32), the following relation can be derived:

$$k' = \frac{k}{y^{n+1}} \tag{35}$$

Eqs. (34) and (35) together offer a means for converting the hardening parameters for the Tex–Iso model from those for the Von–Iso model.

3. Implementation into elastic-plastic FE simulations

To incorporate the constitutive models described above into an elastic-plastic FE analysis, a three-dimensional user material (UMAT) subroutine was developed and employed in conjunction with the FE code ABAQUS/Standard. This subroutine is mainly composed of three parts, which deal with: (1) the updating of stresses and state-dependent variables, (2) the detection of elastic-plastic transition, and (3) the calculation of the tangent modulus. In this section, the implementation is summarized for the general case, i.e. the Tex–Mic model. For the other three models, the algorithm can be simplified accordingly. In the current implementation, the material frame is assumed to be orthogonal and to rotate according to the continuous spin tensor, i.e. the antisymmetric part of the velocity gradient. Accordingly, the integration of stress-rate is done in the co-rotational material axes.

3.1. Updating of stresses and state-dependent variables

In the displacement-based FE method, the total strain to be applied to the deforming body is divided into small strain increments. In each step of the simulation, the constitutive equations have to be integrated in order to advance the constitutive variables from the preceding equilibrated state. In this work, the implicit backward Euler method is employed, which assumes that the components of the plastic strain-rate remain constant during the increment and equal to the values at the end of the increment.

On one hand, according to the incremental form of the generalized Hooke's law, the stress tensor can be related to the elastic strain tensor by

$$\Delta\boldsymbol{\sigma} = \mathbf{D}^{\mathrm{e}} : \Delta\boldsymbol{\varepsilon}^{\mathrm{e}}, \tag{36}$$

where $\mathbf{D}^{\mathrm{e}}$ is the fourth-order elasticity tensor given by $\mathbf{D}^{\mathrm{e}} = 2G\mathbf{T} + K\boldsymbol{\delta}\otimes\boldsymbol{\delta}$ for the case of isotropic elasticity, with $\mathbf{T} = \mathbf{I} - \boldsymbol{\delta}\otimes\boldsymbol{\delta}/3$ the fourth-order deviatoric operator, G the elastic shear modulus and K the bulk modulus.

Let $[t_n, t_{n+1}]$ be the time interval of interest. The total strain increment $\Delta\boldsymbol{\varepsilon}_i$ between the pervious equilibrium state (at time t_n) and the current configuration (at time t_i, i.e. an intermediate state during the iteration) is defined as the integral of $\dot{\boldsymbol{\varepsilon}}_i$ during the time period. Then, the so-called trial stress (or elastic predictor) is defined by

$$\boldsymbol{\sigma}_i^* = \boldsymbol{\sigma}_n + \mathbf{D}^{\mathrm{e}} : \Delta\boldsymbol{\varepsilon}_i. \tag{37}$$

By decomposing the total strain increment into elastic and plastic parts, i.e. $\Delta\boldsymbol{\varepsilon}_i = \Delta\boldsymbol{\varepsilon}_i^{\mathrm{e}} + \Delta\boldsymbol{\varepsilon}_i^{\mathrm{p}}$, the final stresses $\boldsymbol{\sigma}_i$ at time t_i can be given as:

$$\boldsymbol{\sigma}_i = \boldsymbol{\sigma}_n + \mathbf{D}^{\mathrm{e}} : (\Delta\boldsymbol{\varepsilon}_i - \Delta\boldsymbol{\varepsilon}_i^{\mathrm{p}}) = \boldsymbol{\sigma}_i^* - \mathbf{D}^{\mathrm{e}} : \Delta\boldsymbol{\varepsilon}_i^{\mathrm{p}} \tag{38}$$

and the corresponding deviatoric stress tensor $\hat{\boldsymbol{\sigma}}_i$ becomes:

$$\hat{\boldsymbol{\sigma}}_i = \hat{\boldsymbol{\sigma}}_i^* - 2G\Delta\boldsymbol{\varepsilon}_i^{\mathrm{p}}, \tag{39}$$

where $\hat{\boldsymbol{\sigma}}_i^*$ is the deviatoric trial stress.

On the other hand, as represented by Eq. (13), updated deviatoric stresses should respect the flow rule associated to the plastic potential and pertain to the yield locus defined by the updated state variables. Then, the equality of the deviatoric stresses as given by Eqs. (13) and (39) respectively, leads to:

$$\mathbf{X}_i + \tau_i \frac{\partial\Gamma(\Delta\boldsymbol{\varepsilon}_i^{\mathrm{p}})}{\partial\Delta\boldsymbol{\varepsilon}_i^{\mathrm{p}}} - (\hat{\boldsymbol{\sigma}}_i^* - 2G\Delta\boldsymbol{\varepsilon}_i^{\mathrm{p}}) = 0. \tag{40}$$

Therefore, the problem of integrating the constitutive equations reduces to finding the unknown plastic strain increment $\Delta\boldsymbol{\varepsilon}_i^{\mathrm{p}}$ (5 independent unknowns) by solving iteratively this non-linear equation system. The stresses and state-dependent variables can then be updated using the solved $\Delta\boldsymbol{\varepsilon}_i^{\mathrm{p}}$.

3.2. Detection of elastic–plastic transition

During a FE simulation, the yield locus must be consulted in order to find the transition from the elastic to the plastic region, or in order to detect a return to the elastic region. The integration scheme as described above is invoked only when the trial stress is beyond the yield locus.

However, this detection is not straightforward with the current strain-rate space formulation since it is not possible to analytically convert an equation known in strain-rate space into an equation in stress space, i.e. there is no explicit expression of the yield function. In this case, the yield locus point corresponding to a given

stress direction has to be found by means of a minimization technique as explained by Van Houtte et al. (1989). For rate-insensitive and plastically incompressible materials, this minimization procedure is a four-dimensional problem since the stress associated to the plastic strain-rate $\dot{\boldsymbol{\varepsilon}}^{\mathrm{p}}$ depends only on its direction $\mathbf{A}$, which can be represented by a set of four independent variables. Hoferlin et al. (1999b) have shown that the BFGS algorithm is well suited for this procedure.

3.3. Consistent tangent modulus

The implicit FE strategy requires the formulation of the element stiffness matrix, which gives the variation of each component of the energetically internal forces with respect to each degree of freedom of the element's nodes. When a co-rotational formulation is used for the numerical integration of the constitutive law, the construction of the element stiffness matrix in the global axes needs among other things the tangent modulus in the co-rotational axes, which is defined as the linearization of the co-rotational stresses. In this section, we derive analytically the consistent tangent modulus, in the sense that it is in consistent with the integration scheme used for the updating of the Cauchy stresses.

Firstly, the differentiation of Eq. (38) gives

$$\mathrm{d}\boldsymbol{\sigma}_i = \mathbf{D}^{\mathrm{e}} : (\mathrm{d}\boldsymbol{\varepsilon}_i - \mathrm{d}\Delta\boldsymbol{\varepsilon}_i^{\mathrm{p}}). \tag{41}$$

Then, the material time derivative of the dual form of the flow rule [Eq. (13)] according to the consistency condition, yields:

$$\begin{aligned} \mathrm{d}\hat{\boldsymbol{\sigma}}_i &= \frac{\partial(\mathbf{X}_i + \tau_i \mathbf{U}_i)}{\partial \Delta\boldsymbol{\varepsilon}_i^{\mathrm{p}}} \mathrm{d}\Delta\boldsymbol{\varepsilon}_i^{\mathrm{p}} \\ &= \left\{ \frac{\partial \boldsymbol{X}_i}{\partial \Gamma_i} \frac{\partial \Gamma(\Delta\boldsymbol{\varepsilon}_i^{\mathrm{p}})}{\partial \Delta\boldsymbol{\varepsilon}_i^{\mathrm{p}}} + \frac{\partial \tau_i}{\partial \Gamma_i} \frac{\partial \Gamma(\Delta\boldsymbol{\varepsilon}_i^{\mathrm{p}})}{\partial \Delta\boldsymbol{\varepsilon}_i^{\mathrm{p}}} \otimes \frac{\partial \Gamma(\Delta\boldsymbol{\varepsilon}_i^{\mathrm{p}})}{\partial \Delta\boldsymbol{\varepsilon}_i^{\mathrm{p}}} + \tau_i \frac{\partial^2 \Gamma(\Delta\boldsymbol{\varepsilon}_i^{\mathrm{p}})}{\partial \Delta\boldsymbol{\varepsilon}_i^{\mathrm{p}} \partial \Delta\boldsymbol{\varepsilon}_i^{\mathrm{p}}} \right\} : \mathrm{d}\Delta\boldsymbol{\varepsilon}_i^{\mathrm{p}} \end{aligned} \tag{42}$$

Replacing the term within the parentheses on the right-hand side by the fourth-order plastic modulus tensor $\mathbf{D}_i^{\mathrm{p}}$, (42) can be simplified to

$$\mathrm{d}\hat{\boldsymbol{\sigma}}_i = \mathbf{D}_i^{\mathrm{p}} : \mathrm{d}\Delta\boldsymbol{\varepsilon}_i^{\mathrm{p}}, \tag{43}$$

where

$$\mathbf{D}_i^{\mathrm{p}} = \mathbf{B}_i \mathbf{U}_i + H_i \mathbf{U}_i \otimes \mathbf{U}_i + \tau_i \mathbf{V}_i. \tag{44}$$

Here, $\mathbf{B}_i$ denotes the plastic hardening modulus associated with the kinematic hardening at time t_i, which can be written, using Eqs. (16) and (17), as

$$\mathbf{B}_i = \frac{\partial \mathbf{X}_i}{\partial \Gamma_i} = C_{\mathrm{X}}(X_{\mathrm{sat}} \mathbf{U}_i - \mathbf{X}_i). \tag{45}$$

H_i denotes the plastic hardening modulus associated with the isotropic hardening at time t_i, which can be derived, using Eqs. (21), (24) and (25), as

$$H_i = \frac{\partial \tau_i}{\partial \Gamma_i} = C_{\mathrm{R}}(R_{\mathrm{sat}} - R_i) + \frac{m}{\sqrt{S_{\mathrm{D}}^2 + S_{\mathrm{L}}^2}} \left\{ C_{\mathrm{SD}} S_{\mathrm{D}} [h_{\mathrm{P}}(S_{\mathrm{sat}} - S_{\mathrm{D}}) - h_{\mathrm{X}} S_{\mathrm{D}}] - C_{\mathrm{SL}} S_{\mathrm{L}} \left(\frac{S_{\mathrm{L}}}{S_{\mathrm{sat}}} \right)^{n_{\mathrm{L}}} \right\} \tag{46}$$

The fourth-order tensor $\mathbf{V}_i$ denotes simply the second-order term in (42), i.e.

$$\mathbf{V}_i = \frac{\partial^2 \Gamma(\Delta \boldsymbol{\varepsilon}_i^{\mathrm{p}})}{\partial \Delta \boldsymbol{\varepsilon}_i^{\mathrm{p}} \partial \Delta \boldsymbol{\varepsilon}_i^{\mathrm{p}}}. \tag{47}$$

Replacing $\mathrm{d}\hat{\boldsymbol{\sigma}}_i$ by $d\boldsymbol{\sigma}_i$ using the fourth-order deviatoric operator $\mathbf{T}$, (43) can be rewritten as

$$\mathbf{T} : \mathrm{d}\boldsymbol{\sigma}_i = \mathbf{D}_i^{\mathrm{p}} : \mathrm{d}\Delta \boldsymbol{\varepsilon}_i^{\mathrm{p}}. \tag{48}$$

Finally, substituting Eq. (48) into Eq. (41), after some manipulation, we obtain

$$\mathrm{d}\boldsymbol{\sigma}_i = \mathbf{D}_i^{\mathrm{ep}} : \mathrm{d}\boldsymbol{\varepsilon}_i, \tag{49}$$

where

$$\mathbf{D}_i^{\mathrm{ep}} = \left(\mathbf{D}^{\mathrm{e}^{-1}} + \mathbf{T} : \mathbf{D}_i^{\mathrm{p}^{-1}} \right)^{-1} \tag{50}$$

represents the consistent tangent modulus tensor. Clearly, this expression gives the variation of the co-rotational Cauchy stresses induced by the change in the co-rotational strain increment.

Noted that for the part related to the plastic potential, the basic principles for the derivation of the consistent tangent modulus are similar to those presented by Szabó and Jonas (1995). It is also worth noting that the relevant five-dimensional stress and strain vectors used in the manipulation of the present plastic potential must be transformed into their six-dimensional forms during the calculations as described above.

4. Applications

4.1. Material

An interstitial-free (IF) steel sheet of 0.8 mm thickness has been used in the present investigation. To determine the initial texture of the sheet, four incomplete

pole figures, namely (110), (200), (211) and (310), were measured by means of X-ray diffraction. Then, the ODFs were calculated from the pole figures using Bunge's method (Bunge, 1982). This procedure was conducted at seven depths of the sheet, in order to calculate the average texture through the thickness of the sheet.

The ODFs of the average texture thus obtained are depicted in Fig. 1(a) by the $\varphi_2 = 45^\circ$ section, from which the main texture components can be seen. It shows that a strong γ-fiber ($<111>$//ND, the normal direction) with noticeable spread along the so-called α-fiber ($<110>$//RD) has well developed in this material. The texture data were then used to determine the coefficients of the plastic potential, using a 6th-order series expansion [see Eq. (8)]. The potential slip systems considered in the calculations are the $\{110\}+\{112\}<111>$ families with $\tau_{\{110\}} = \tau_{\{112\}}$. As shown in Fig. 1(b), the yield locus derived from the plastic potential fits very well to the one calculated directly by use of the TBH crystal plasticity model.

Table 1 lists the material parameters identified for the four constitutive models according to the procedures as explained in Section 2.4. Values of 210,000 MPa and 0.3 for the Young's modulus and the Poisson's ratio respectively were employed in the following simulations.

4.2. FE simulations of cup drawing

4.2.1. Cup drawing test

The cup drawing test has been performed on a hydraulic press with a blank diameter of 100 mm, a punch diameter of 50 mm, a punch fillet radius of 5 mm, a die opening of 52.5 mm and a die fillet radius of 10 mm. A Molykote Metalform lubricant was applied on the blank and the tools. The test was performed with blankholder force of 12 kN. The cup profiles, i.e. cup height as a function of the

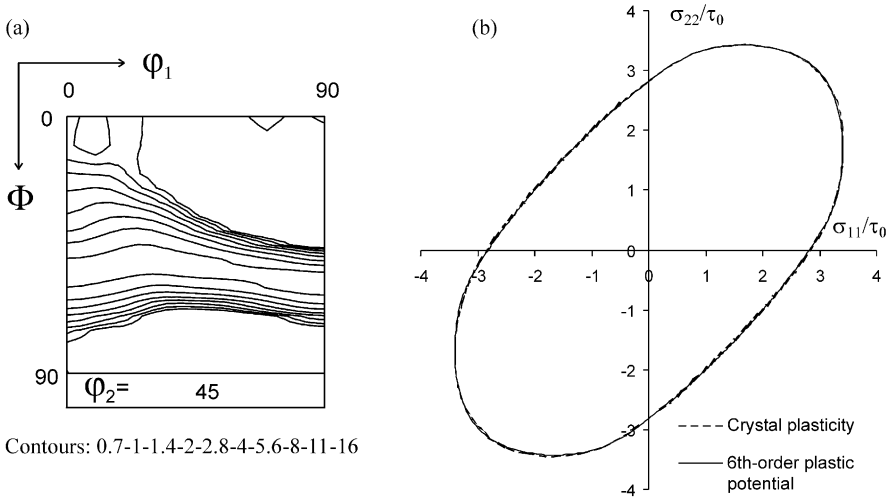

Fig. 1. (a) Initial texture of the IF steel sheet, and (b) the corresponding σ_{11}/τ_0–σ_{22}/τ_0 sections of the normalized yield loci calculated by crystal plasticity and generated from the plastic potential, respectively.

Table 1
Material parameters of the IF steel identified for the four constitutive models

Von–Iso	$k = 530.4$ MPa, $\varepsilon_0^p = 0.00159$, $n = 0.2596$												
Tex–Iso	$k' = 143.6$ MPa, $\Gamma_0 = 0.00449$, $n = 0.2596$												
	C_P	C_R	C_{SD}	C_{SL}	C_X	m	n_L	n_P	λ	τ_0 (MPa)	R_{sat} (MPa)	S_{sat} (MPa)	X_0 (MPa)
Von–Mic	3.30	26.94	5.35	13.45	24.98	0.6	1.88	27.1	3.93	114.9	78.4	234.2	13.7
Tex–Mic	1.17	9.55	1.90	4.77	8.86	0.6	1.88	27.1	3.93	40.73	27.79	83.02	4.86

angle to RD, were measured manually at an interval of 15° and averaged over the symmetrically equivalent positions.

4.2.2. FE simulations

The cup drawing test described above was simulated using ABAQUS, in conjunction with the UMAT subroutine developed for the constitutive models as described in Section 3. Considering the orthorhombic sample symmetry and the axisymmetry of the tools, only one quarter of the blank (and the tools) was used in the FE model, as shown in Fig. 2. The blank was represented by means of 531 eight-node linear brick elements with reduced integration and hourglass control (element type C3D8R). The tools were represented by use of a total of 648 four-node three-dimensional rigid surface elements (element type R3D4). The 1, 2 and 3 axes of the global coordinate system were aligned with the RD, TD (transverse direction), and ND of the sheet, respectively. The Coulomb friction coefficient between the blank and the tools was prescribed as 0.10. To overcome the classical convergence problem when the major part of the flange is drawn into the die opening, the position of the blankholder is fixed before such convergence problem arises.

4.2.3. Results and discussions

In a circular cup drawing operation, the texture-induced anisotropy can most easily be seen from the earing behavior. To this end, the cup profiles predicted by use of the four plasticity models are compared against the experimental results in Fig. 3. It can be seen that the experimental 0/90°-type earing behavior for the

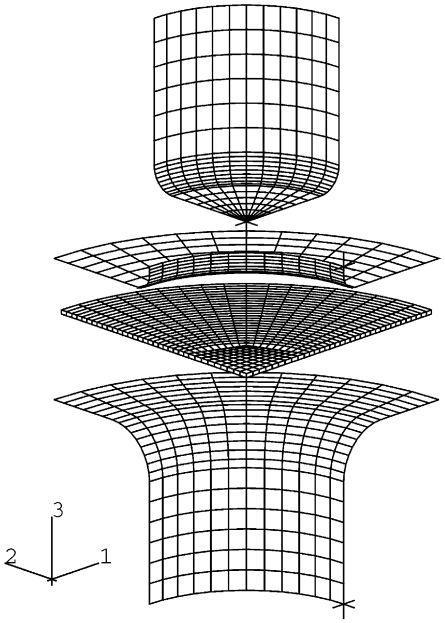

Fig. 2. Exploded view of the FE mesh used in the cup drawing simulations.

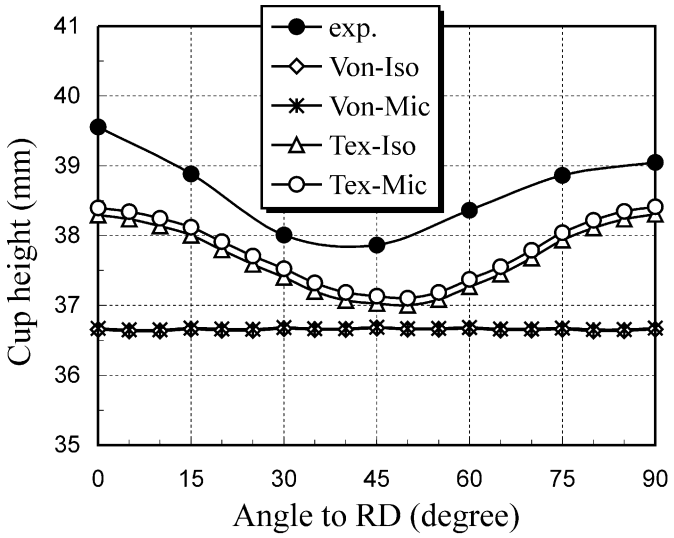

Fig. 3. Comparison of measured and predicted cup profiles.

material is well reproduced in the predictions of the Tex–Mic and the Tex–Iso models, although in the experiment the ear at 0°-direction is slightly higher than that at 90° while the predictions show almost equal ear heights at both directions. The two models based on the von Mises yield formulation (Von–Iso and Von–Mic) of course cannot predict the earing behavior.

Fig. 3 also shows that the cup height is underestimated in all the predictions, indicating the friction coefficient as employed in the present simulations is too low. Nevertheless, it is also of interesting to see that the cup heights as predicted by the Tex–Iso and the Tex–Mic models are more closer to the experimental one as compared to those obtained by the Von–Iso and the Von–Mic models. This indicates that the consideration of texture is necessary not only for capturing the earing behavior, but also for a better reproduction of the cup height. The latter usually implies also better prediction of the thickness distribution in the cup.

On the other hand, the advantage of the microstructural hardening model as compared to the isotropic hardening law appears to be not significant in this case. This is evident from the minor difference in the predictions between the Tex–Mic and the Tex–Iso models, and also in the predictions between the Von–Mic and the Von–Iso models. This might be due to the fact that there are no abrupt strain-path changes in such kind of deep drawing operations, although continuous strain-path changes do happen when the flange of the blank passes over the radius of the die.

Table 2 shows the CPU times of the cup drawing simulations, obtained on a SUN workstation with a 300 MHz UltraSPARC-II processor. The CPU time for using the Tex–Mic model is about 3 times that for the Von–Iso model, and is only about 5% more expensive as compared to the Tex–Iso model. It thus indicates that the increase of the computer cost is mainly caused by the texture-related calculations. Note that the CPU time difference as shown in this table between the Von–Mic and

Table 2
CPU times for the cup drawing simulations using different constitutive models

	Von–Iso	Von–Mic	Tex–Iso	Tex–Mic
CPU (min)	109	184	256	266

the Von–Iso models does not indicate the relevance of the CPU cost with the hardening models. In the present study, the simulation with the Von–Mic model was performed as a special case of the Tex–Mic model, in the sense that a random texture was employed to produce the von Mises yield locus. Meanwhile, the CPU time difference between the Von–Mic and the Tex–Mic models demonstrates in fact the influence of the texture intensity on the computation time.

4.3. FE simulations of sequential test

4.3.1. Sequential test

A sequential test has been designed (Reis et al., 2001) to measure the plastic anisotropy under pseudo-orthogonal strain-path change. It involves two different strain paths: (1) prestrain in balanced biaxial stretching obtained by bulge test with a circular die; and (2) reloading in uniaxial tension along RD on a sample cut from the bulged sheet. Firstly, a hydraulic bulge test was performed to apply balanced biaxial stretching deformation on the initial material. The bulge test equipment consists of a hydraulic blankholder, a die, and a hydraulic power supply, as illustrated in Fig. 4(a). The bulge sample is a circular blank with diameter of 250 mm. The hydraulic bulge pressure was imposed at a rate of 0.1 MPa/s. The test was performed to a dome height (h_D) equal to 25 mm and then unloaded. A clamping force was applied in order to avoid sliding of the sample. A grid of circles with diameter of 5 mm was electrochemically printed on the surface of the initial sample. Strains were calculated from measurements of the deformed grids using a NC Profile Projector.

The sample for uniaxial tensile test was cut from the center of the bulged sample with the longitudinal direction parallel to RD, as shown in Fig. 4(b). The uniaxial tensile test was conducted on an Instron-4507 machine equipped with a high resolution digital automatic extensometer. The gauge length is 50 mm and the crosshead speed is 5 mm/min. The strains were calculated from the electrochemically-printed circle grids with initial diameter of 2.5 mm. The onset of localized necking was determined from strain distribution profiles near the necking region using the Bragard method.

4.3.2. FE simulations

The sequential test described above was simulated using the four constitutive models as described in Section 2.4. In light of the orthorhombic sample symmetry and the axisymmetry of the tools, only one quarter of the blank was used in the FE model. For simplification purposes, the FE model for the bulge test consists of only the blank and the die (Fig. 5). The effective diameter of the blank is taken to be 190

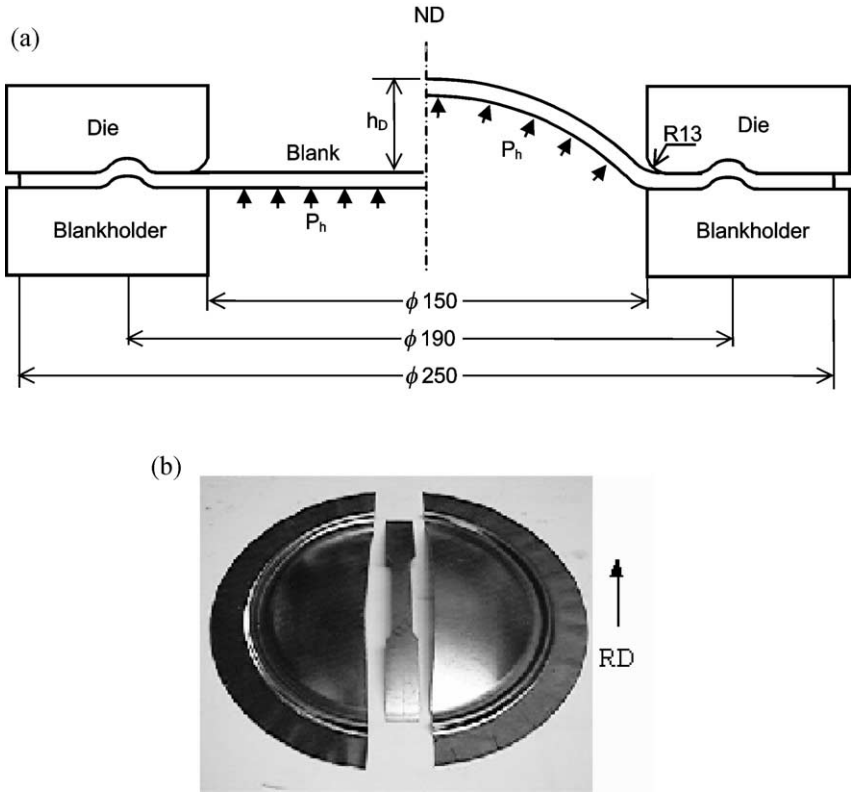

Fig. 4. Illustrations of (a) the bulge test and (b) the extraction of the tensile sample from the bulged sample. All dimensions are in mm.

mm where the drawbeads are imposed in the experiment [see Fig. 4(a)]. The blank was represented by means of 1240 C3D8R elements. The 1, 2 and 3 axes of the global coordinate system were aligned with the RD, TD, and ND of the sheet, respectively. The die was represented by a total of 180 R3D4 elements. The friction effects were neglected. The role of the drawbeads during loading was implemented by fixing all the nodes at the periphery of the blank. The hydraulic bulge pressure was imposed on the lower surface of the blank.

Two sets of bulge simulations have been performed. In the first set, the simulation of the loading step was performed up to the reaching of the experimental dome height (25 mm), in order to inspect the behavior of the four constitutive models in the bulge deformation alone. The predicted maximum pressure during loading and the strain distribution after unloading will be compared with the experimental results. In the second set of simulations, for the purpose of examining the post-bulge differences, the loading step was simulated up to a certain dome height, whenever the magnitude of plastic strain at the dome after unloading is equal to the experimental one (12%). The latter set of simulations was then followed by uniaxial tension to complete the sequential test. This ensures that the samples employed for the

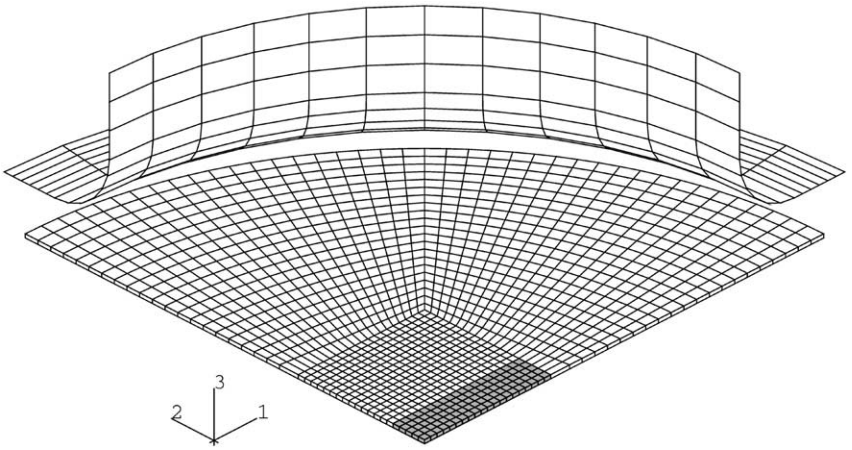

Fig. 5. Exploded view of the FE mesh used in the simulations of the bulge test. The sample to be used in the subsequent uniaxial tensile simulation is indicated in grey.

tensile simulations have the same magnitude of prestrain, at least at the center of the samples. In both sets of bulge simulations, the unloading step was simulated by reducing the hydraulic bulge pressure to zero. The CPU ratios between the different constitutive models in the bulge simulations are similar to those found for the cup drawing simulations.

In the simulation of the tensile test, only the portion of the specimen within the gauge length was considered. Again, in light of the orthorhombic sample symmetry, only one quarter of the blank was used in the FE model. A tensile sample with 20 (along RD)×5 (along TD) elements was extracted from the center of the bulged specimen, as indicated in Fig. 5. Their initial x- and y-coordinates (before bulge simulation) were reactivated in order to get a regular mesh. The tensile sample thus defined corresponds exactly to the in-plane dimension of one quarter of the real tensile sample, i.e. 25.0×6.25 mm. Meanwhile, the z-coordinates were set to zero for the nodes on the lower surface, and set to the thickness after the bulge simulation for those on the upper surface, in order to keep the thickness distribution after the bulge simulation. Since the strains after bulging are small, it is fair to neglect the displacement of the integration points of the elements. Hence the initial values of the state variables in the tensile simulation were simply taken at the integration points of the corresponding elements after the bulge simulation, and no special interpolation was performed. The tensile simulation was carried out by imposing the same longitudinal displacement on the nodes located at the extremities of the tensile sample, without transverse freedom.

4.3.3. Results and macroscopic discussions

The accuracy of the models in the prediction of hydraulic pressure and strain distribution in the bulge test can be evaluated using the first set of bulge simulations. The simulation results of the maximum hydraulic pressure $P_h^{\max}$ during loading and

the equivalent plastic strain $\bar{\varepsilon}_{\mathrm{vm}}$ at the dome after unloading are compared against the experimental data in Table 3. It can be seen that the $P_h^{\max}$ and $\bar{\varepsilon}_{\mathrm{vm}}$ values predicted by the Von–Iso model are quite different to the measured ones. The prediction of $\bar{\varepsilon}_{\mathrm{vm}}$ is only very slightly improved by the Von–Mic model. With the Tex–Iso model, a much better agreement between the predicted and the measured $P_h^{\max}$ and $\bar{\varepsilon}_{\mathrm{vm}}$ values has been obtained. Further improvement of the predictions, although small, has been achieved by use of the Tex–Mic model.

The effect of strain-path change in the sequential test can be assessed by comparison between the monotonic and postbiaxial tensile curves. The experimental curves are compared against the predictions of the Von–Iso model in Fig. 6(a), and the Tex–Mic and the Von-Mic models in Fig. 6(b). In both figures, the postbiaxial curves have been shifted to the right by an amount equal to the effective prestrain, i.e. 12%. Firstly, the experimental results show that the prestrain in the bulge test leads to a higher reloading stress at the beginning of the second tensile straining. Consequently, the experimental tensile specimen suffers from an almost direct rupture at $\varepsilon_{11} = 0.9\%$ of the second straining, due to the strain-path induced softening. As expected, the reloading yielding stress as predicted by the Von–Iso model is almost the same as that obtained for the monotonic tensile test on the as-received material, showing no effect of the strain-path change [Fig. 6(a)]. Meanwhile, the Von–Iso prediction indicates necking at $\varepsilon_{11} = 14.3\%$ for the tensile test on the prestrained material, which is completely erroneous. Although not plotted here, similar results have been obtained with the Tex–Iso model.

In contrast, the prediction of the Tex–Mic model reproduces correctly the experimental higher reloading stress after the strain-path change [Fig. 6(b)]. It also shows clearly a work-stagnation starting at $\varepsilon_{11} = 1.4\%$, followed by softening at $\varepsilon_{11} = 2.6\%$, during the second straining. This corresponds well to the strain level where the premature failure occurs in the experimental postbiaxial tensile test. Similar prediction has been obtained with the Von–Mic model [Fig. 6(b)]. However, as compared to the Tex–Mic model, the Von–Mic model predicts only a stagnation of the flow stress instead of softening during the second straining. This difference is more distinguishable by looking at the evolution of the hardening rate ($\Theta = \mathrm{d}\sigma_{11}/\mathrm{d}\varepsilon_{11}$), which are also plotted in this figure. It is clear that the minimum Θ value as predicted by the Tex–Mic model is negative, whereas that predicted by the Von–Mic model is not.

The transient hardening effect as stated above is attributed to the pseudo-orthogonal strain-path change during this sequential test. According to Schmitt et al. (1985), a strain-path change can be characterized by use of a parameter θ, defined as $\theta = \cos\alpha = \mathbf{A}^1 : \mathbf{A}^2$, where $\mathbf{A}^1$ and $\mathbf{A}^2$ denote, respectively, the directions of the

Table 3
Maximum hydraulic pressure ($P_h^{\max}$) during loading and equivalent plastic strain ($\bar{\varepsilon}_{\mathrm{vm}}$) at the dome of the bulged sample after unloading in the bulge test

	Experimental	Von–Iso	Von–Mic	Tex–Iso	Tex–Mic
$P_h^{\max}$ (MPa)	3.20	2.75	2.76	2.94	2.96
$\bar{\varepsilon}_{\mathrm{vm}}$	0.120	0.130	0.124	0.124	0.118

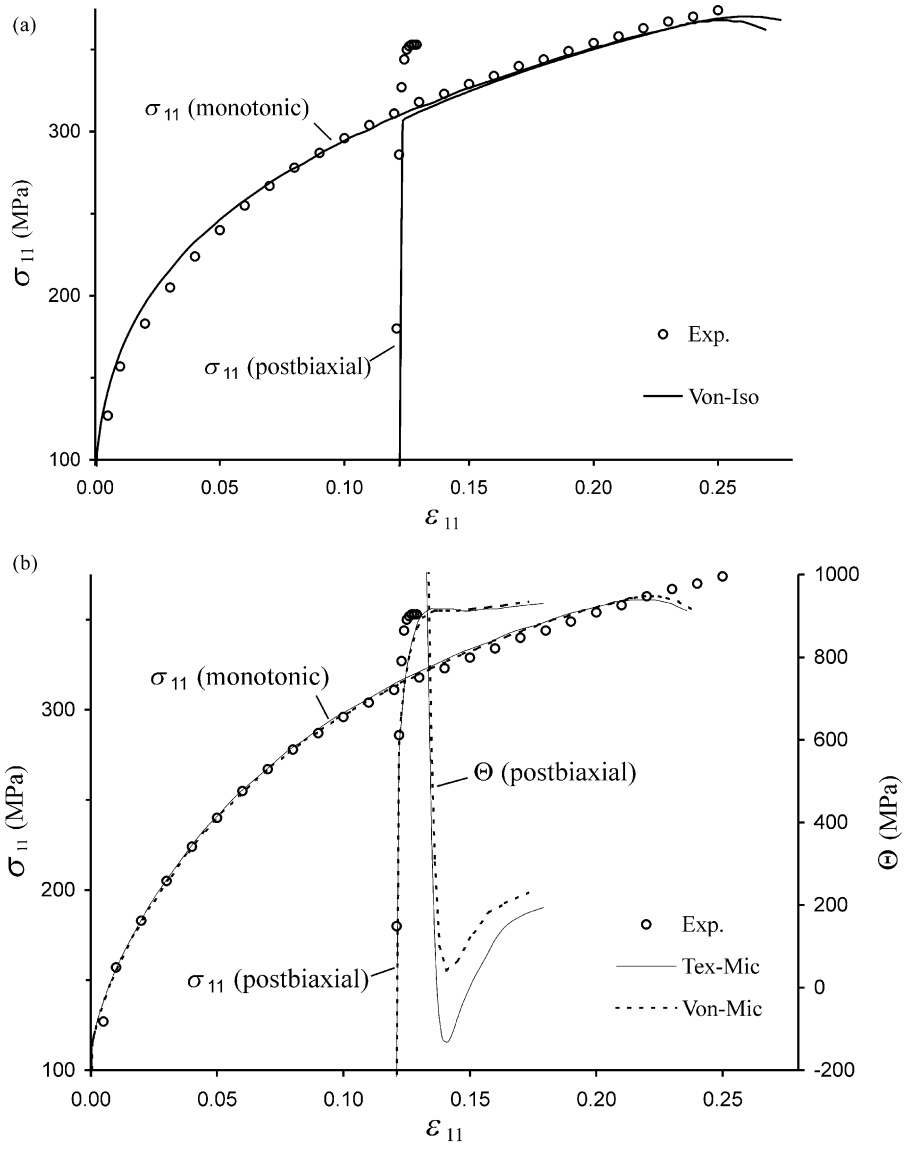

Fig. 6. Comparisons of the experimental monotonic and postbiaxial true stress–true strain tensile curves with the predictions obtained by using the (a) Von–Iso model, (b) Tex–Mic and Von–Mic models. The evolution of the hardening rate ($\Theta = d\sigma_{11}/d\varepsilon_{11}$) derived from the postbiaxial tensile curves are also plotted in (b) to illustrate more clearly the difference between the predictions of the two models.

plastic strain-rate tensors for the first and the second deformation stages. It is evident from this definition that θ varies from 1 ($\alpha = 0°$, monotonic test) to -1 ($\alpha = 180°$, Bauschinger test). A deformation sequence is orthogonal when $\theta = 0$ ($\alpha = 90°$). For the present sequential test, the θ value equals to 0.5 ($\alpha = 60°$) when the texture

effect is excluded (in Von–Mic), and equals to 0.28 ($\alpha = 73.7°$) when the texture effect is included (in Tex–Mic). The latter implies a strain-path change that is more close to an orthogonal one. This explains the relative stronger cross effect in the prediction of the Tex–Mic model than that of the Von–Mic model as stated above. Nevertheless, the texture aspect is clearly less important than the microstructural hardening or softening in this case.

4.3.4. Microscopic discussions

To discuss the physical cause of the macroscopically observed plastic anisotropy under the strain-path change, it is useful to investigate the evolution of the main state variables in the simulation. For the current simulation of the sequential test, using the Tex–Mic model, the premature necking has happened very soon after the strain-path change, and therefore the evolution of the state variables can only be extracted up to a very limited amount of the second straining. For this reason, another simulation has been performed using only one element, which follows the strain history of the material at the center of the sample used in the sequential test, i.e. 12% prestrain in bulge deformation followed by uniaxial tension along RD. In this case, there is no limitation of the maximum strain amount in the simulation of the second straining. It thus allows the discussion of the evolution of the state variables up to a sufficiently large strain in the second deformation stage.

Fig. 7 shows the evolution of the state variables thus obtained using the Tex–Mic model. Recall that in this model, both isotropic and kinematic hardening contribute to the transient hardening. The isotropic hardening is represented by τ. As indicated in Eq. (25), the first contribution to the evolution of τ is from the variable R, which is related to the statistically accumulated dislocations. The value R increases very rapidly and approaches almost the saturation value at the end of the prestrain. The strain-path change does not lead to any transient in the evolution of R [Fig. 7(a)].

Then, it is of interest to inspect the evolution of the directional strength of dislocation structures $\mathbf{S}$, which contributes to both the isotropic and the kinematic hardening. The evolution of $\mathbf{S}$ consists of two aspects: $\mathbf{S}_L$ and S_D. As shown in

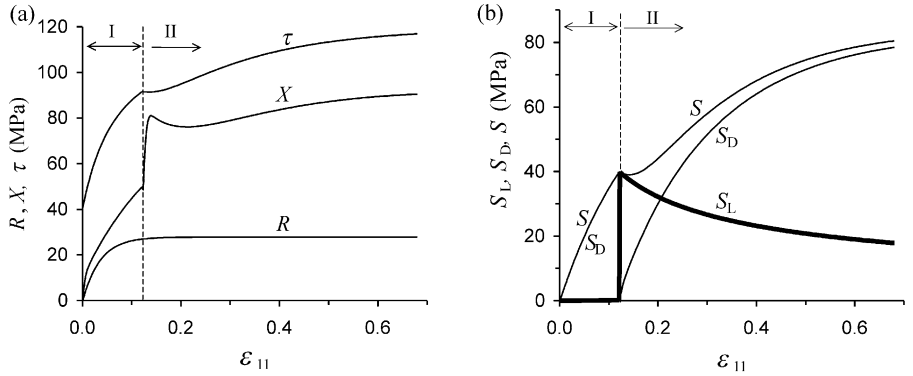

Fig. 7. Evolution of state variables at the center of the sample during the sequential test (I: biaxial stretching; II: uniaxial tension), as predicted by the Tex–Mic model: (a) R, X, τ; (b) S_L, S_D, S.

Fig. 7(b), the value S_L (the norm of $\mathbf{S}_L$) remains zero at the first stage of the sequential test, and it appears only when the strain-path has changed. It decreases rather rapidly in the second straining. Meanwhile, the value S_D increases continuously during the first straining and jumps to zero at the beginning of the second strain path. Afterwards, it increases with the second strain and tends to approach its saturation value S_{sat}. As a result of the decrease of S_L, the evolution of S (the norm of $\mathbf{S}$) presents a slight loss at the transition of strain-path [Fig. 7(b)]. This contributes directly to the transient of isotropic hardening at the beginning of the second straining, as indicated by the decrease of τ [Fig. 7(a)]. With the further increase of the second straining, the increasing in the rate of S_D becomes higher than the decrease in the rate of S_L. As a result, S and therefore τ increase again. As R and S_D approaching to their saturation values at large second strain, the increase in the rate of τ decreases again (Fig. 7).

On the other hand, the kinematic hardening is indicated by the evolution of the backstress $\mathbf{X}$, and is associated with the process of dislocation pile-up. As represented by its norm X [Fig. 7(a)], the backstress increases rapidly during the first straining, although the rate of increase is decreasing. After the transition of strain-path, it presents still a very high rate of increase. Then, with the further straining in the second path, it starts to decrease, more rapidly as compared to τ. This is due to the relative stronger contribution of the latent dislocations as compared to that of the current active dislocations. Later on, X increases again due to the strong increase of S_D. The evolution of τ and $\mathbf{X}$ together, as indicated in Eq. (13), explains the evolution of the flow stress in Fig. 6(b).

The above discussions indicate that the latent part of the PDS influences the transient hardening and hence the formability under strain-path changes. The experimental investigations of Rauch and Schmitt (1989) might be a possible microscopic interpretation of the strain-path induced anisotropy for the present sequential test. They suggested that the interaction between the currently active slip systems and the previously formed dislocation structure causes cross hardening and is followed by microband formation which leads to a decrease in the hardening rate or even softening. For the present material, the Von–Mic model predicts a strain-path change with larger θ value than that obtained by the Tex–Mic model. Consequently, the prediction of the Von–Mic model implies a smaller latent part of dislocation structure after the strain-path change and, therefore, underestimates the transient hardening effect.

5. Conclusions

FE simulations of sheet metal forming have been performed using the texture- and microstructure-based (Tex–Mic) constitutive model. The model is interrogated for its predictive capabilities by comparing FE simulations against experimental results for the circular cup drawing and the pseudo-orthogonal sequential test using the IF steel sheet. The following conclusions can be drawn from this investigation.

(1) The present model is capable of predicting the plastic anisotropy induced by texture and strain-path change in sheet metal forming. This is demonstrated by the

satisfactory predictions of the earing behavior in the cup drawing test, the maximum hydaulic pressure and plastic strain in the bulge-stage of the sequential test, and the transient hardening effects in the sequential test.

(2) Comparisons of the predictions obtained with the present and the other simple models indicate that, it is essential to take into account the influence of texture in simulations of simple forming processes such as deep drawing and bulge forming. In such processes, the further incorporation of the microstructural anisotropic hardening effects can improve the accuracy of the simulations, although in a less significant degree. On the other hand, the incorporation of the microstructual hardening effects is more important for multiple-stage forming processes, in order to capture the significant changes of the formability of the material under abrupt strain-path changes. In this case, the consideration of texture is still of importance, since the magnitude of the strain-path change is related directly to the texture of the material.

(3) The CPU time for a simulation with the present model usually increases only by a factor of about 3 as compared to the conventional von Mises model with isotropic hardening. It is therefore feasible to apply the present model in simulations of realistic forming processes.

Acknowledgements

The authors acknowledge the European Community for the financial support through the Brite-EuRam project (Contract No. BRPR-CT97-0492). They are also grateful to I. De Rycke (OCAS, Belgium) for supplying the material and J.F. Duarte (University of Porto, Portugal) for providing the experimental data for the sequential test.

References

Arminjon, M., Bacroix, B., 1991. On plastic potentials for anisotropic metals and their derivation from the texture function. Acta Mech. 88, 219–243.

Bay, B., Hansen, N., Hughes, D.A., Kuhlmann-Wilsdorf, D., 1992. Evolution of f.c.c. deformation structure in poyslip. Acta Metall. 40, 205–219.

Beaudoin, A.J., Mathur, K.K., Dawson, P.R., Johnson, G.C., 1993. Three-dimensional deformation process simulation with explicit use of polycrystalline plasticity models. Int. J. Plasticity 9, 833–866.

Becker, R., Smelser, R.E., Panchanadeeswaran, S., 1993. Simulation of earing in aluminium single crystals and polycrystals. Modelling Simul. Mater. Sci. Eng. 1, 203–224.

Bunge, H.-J., 1982. Texture Analysis in Materials Science. Butterworths, London.

Chung, K., Shah, K., 1992. Finite element simulations of sheet metal forming for planar anisotropic metals. Int. J. Plasticity 8, 453–476.

Ghosh, A.K., Backofen, W.A., 1973. Strain-hardening and instability in biaxially stretched sheets. Metall. Trans. 4, 1113–1123.

Haddadi, H., Bouvier, S., Teodosiu, C. 1999. Experimental study of hardening behavior—identification of the microstructural model. Twelve-Monthly Progress Report of the CASHFORM Project (Brite-EuRam Contract No. BRPR-CT97-0492): Annex III.

Hiwatashi, S., Van Bael, A., Van Houtte, P., Teodosiu, C., 1997. Modelling of plastic anisotropy based on texture and dislocation structure. Comp. Mater Sci. 9, 274–284.

Hiwatashi, S., Van Bael, A., Van Houtte, P., Teodosiu, C., 1998. Prediction of forming limit strains under strain-path changes: application of an anisotropic model based on texture and dislocation structure. Int. J. Plasticity 14, 647–669.

Hoc, T., Forest, S., 2001. Polycrystal modelling of IF-Ti steel under complex loading path. Int. J. Plasticity 17, 65–85.

Hoferlin, E., Van Bael, A., Van Houtte, P., Teodosiu, C., 1999a. An accurate model of texture and strain-path induced anisotropy. In: Gélin, J.C., Picart, P. (Eds.), Proc. of the 4th Int. Conf. and Workshop on Numerical Simulation of 3D Sheet Forming Processes. University of Franche-Comté and ENSMM Besançon, Burs, pp. 91–96.

Hoferlin, E., Van Bael, A., Van Houtte, P., 1999b. Comparison between stress-based and strain-based elasto-plastic models for anisotropic metals. In: Khan, A.S. (Ed.), Constitutive and damage modeling of inelastic deformation and phase transformation, Proc. of Plasticity'99. Neat Press Fulton, Maryland, pp. 145–148.

Hoferlin, E., Li, S., Van Bael, A., Van Houtte, P., 2001. Texture- and microstructure-induced anisotropy: micro-macro modelling, implementation. In: Mori, K. (Ed.), Simulation of Materials Processing: Theory, Methods and Applications, Proc. of Inter. Conf. Numiform 2001. Swets & Zeitlinger, Lisse, pp. 209–214.

Hu, Z., 1994. Work-hardening behavior of mild steel under cyclic deformation at finite strains. Acta Metall. Mater. 42, 3481–3491.

Kalidindi, S.R., Bronkhorst, C.A., Anand, L., 1992. Crystallographic texture evolution in bulk deformation processing of metals. J. Mech. Phys. Solid 40, 537–569.

Langlois, L., Berveiller, M., in press. Overall softening and anisotropy related with the formation and evolution of dislocation microstructures. Int. J. Plasticity.

Li, S., Hoferlin, E., Van Bael, A., Van Houtte, P., 2000. Finite element simulation of earing behavior in deep drawing using a texture-based anisotropic strain-rate potential. In: Materials Week 2000 Proceedings, editor and organizer: Werkstoffwoche-Partnerschaft, Frankfurt, 25–28 September 2000, URL: http://www.materialsweek.org/proceedings, Date of download: 06.03.2001.

Li, S., Hoferlin, E., Van Bael, A., Van Houtte, P., 2001. Earing behavior of fcc metals in cup drawing: FE simulations using a texture-based strain-rate potential. In: Mori, K. (Ed.), Simulation of Materials Processing: Theory, Methods and Applications, Proc. of Inter. Conf. Numiform 2001. Swets & Zeitlinger, Lisse, pp. 215–220.

Mathur, K.K., Dawson, P.R., 1989. On modeling the development of crystallographic texture in bulk forming processes. Int. J. Plasticity 5, 69–94.

Rauch, E.F., Schmitt, J.-H., 1989. Dislocation substructures in mild steel deformed in simple shear. Mater Sci. Eng. A113, 441–448.

Rauch, E.F., Thuillier, S., 1993. Plasticity and unstable flow of mild steel. Archives of Metallurgy 38, 167–177.

Reis, A., Santos, A.D., Duarte, J.F., Li, S., Hoferlin, E., Van Bael, A., Van Houtte, P., Teodosiu, C., 2001. FE prediction and experimental validation of a plasticity model of texture and strain induced anisotropy. In: Duflou J.R. et al. (Eds.), Proc. of Inter. Conf. SheMet 2001, Leuven, pp. 237–246.

Savoie, J., MacEwen, S.R., 1996. A sixth order inverse potential function for incorporation of crystallographic texture into predictions of properties of aluminum sheet. Textures Microstruct 26/27, 495–512.

Schmitt, J.H., Aernoudt, E., Baudelet, B., 1985. Yield loci for polycrystalline metals without texture. Mat. Sci. Eng. 75, 13–20.

Szabó, L., Jonas, J.J., 1995. Consistent tangent operator for plasticity models based on the plastic strain-rate potential. Comp. Meth Appl. Mech. Eng. 128, 315–323.

Teodosiu, C., Hu, Z., 1995. Evolution of the intragranular microstructure at moderate and large strains: modelling and computational significance. In: Shen, S.F., Dawson, P.R. (Eds.), Simulation of Materials Processing: Theory, Methods and Applications. Balkema, Rotterdam, pp. 173–182.

Thuillier, S., Rauch, E.F., 1994. Development of microbands in mild steel during cross loading. Acta Metall. Mater. 42, 1973–1983.

Van Bael, A. 1994. Anisotropic Yield Loci Derived from Crystallographic Data and their Application in Finite-element Simulations of Plastic Forming Processes. PhD thesis, Katholieke Universiteit Leuven.

Van Houtte, P., Mols, K., Van Bael, A., Aernoudt, E., 1989. Application of yield loci calculated from texture data. Textures Microstruct. 11, 23–39.

Van Houtte, P., Van Bael, A., Winters, J., Aernoudt, E., Hall, F., Wang, N., Pillinger, I., Hartley, P., Sturgess, C.E.N., 1992. Modelling of complex forming processes. In: Andersen, S.I. et al. (Eds.), Modelling of Plastic Deformation and Its Engineering Applications (Proc. of the 13th Risø Inter. Symp. on Mat. Sci.). Roskilde, Denmark, pp. 161–172.

Van Houtte, P., 1994. Application of plastic potentials to strain rate sensitive and insensitive anisotropic materials. Int. J. Plasticity 10, 719–748.

Zhou, Y., Jonas, J.J., Szabó, L., Makinde, A., Jain, M., MacEwen, S.R., 1997. Incorporation of an anisotropic (texture-based) strain-rate potential into three-dimensional finite element simulations. Int. J. Plasticity 13, 165–181.

Zhou, Y., Jonas, J.J., Savoie, J., Makinde, A., MacEwen, S.R., 1998. Effect of texture on earing in FCC metals: finite element simulations. Int. J. Plasticity 14, 117–138.